

Observation of elastic spin with chiral meta-sources

Weitao Yuan

Tongji University

Chenwen Yang

School of Physics Sciences and Engineering, Tongji University, Shanghai 200092, China

Danmei Zhang

Tongji University

Yang Long

Tongji University

Yongdong Pan

School of Aerospace Engineering and Applied Mechanics, Tongji University

Zheng Zhong

Tongji University

Hong Chen

Tongji University

Jinfeng Zhao

Tongji University

Jie Ren (✉ xonics@tongji.edu.cn)

Tongji University <https://orcid.org/0000-0003-2806-7226>

Article

Keywords: topological phononic devices, applied physics, acoustics

Posted Date: June 15th, 2021

DOI: <https://doi.org/10.21203/rs.3.rs-596912/v1>

License:  This work is licensed under a Creative Commons Attribution 4.0 International License.

[Read Full License](#)

Version of Record: A version of this preprint was published at Nature Communications on November 29th, 2021. See the published version at <https://doi.org/10.1038/s41467-021-27254-z>.

Observation of elastic spin with chiral meta-sources

Weitao Yuan,^{1,2,*} Chenwen Yang,^{1,*} Danmei Zhang,¹ Yang Long,¹ Yongdong Pan,² Zheng Zhong,² Hong Chen,¹ Jinfeng Zhao,^{2,†} and Jie Ren^{1,‡}

¹*Center for Phononics and Thermal Energy Science, China-EU Joint Lab on Nanophononics, Shanghai Key Laboratory of Special Artificial Microstructure Materials and Technology, School of Physics Science and Engineering, Tongji University, Shanghai 200092, China*

²*School of Aerospace Engineering and Applied Mechanics, Tongji University, Shanghai 200092, China*

Directional routing of one-way classical wave has raised tremendous interests about spin-related phenomena in topological metamaterials. This sparks specifically the elastic wave study of synthesizing pseudo-spin degree-of-freedom in meta-structures for implementing topological phononic devices to perform robust elastic wave manipulations. Unlike pseudo-spin in mathematical sense, the physically intrinsic spin angular momentum of elastic wave is predicted quite recently which exhibits selective excitation of unidirectional wave propagation even in conventional solids. However, due to the grand challenge of building up chiral elastic sources, the experimental observation of intrinsic spin of elastic wave and relevant properties is still missing. Here, we successfully measure the elastic spin in two typical elastic modes, i.e. Rayleigh and Lamb waves, by adopting the elaborately designed chiral meta-sources that excite locally rotating displacement polarizations. In both systems, we observe the unidirectional routing of chiral elastic waves, characterize the different elastic spins along different directions, and demonstrate the spin-momentum locking in broad frequency ranges. We also find the selective one-way Lamb wave carries opposite elastic spin on two plate surfaces in addition to the source chirality. The observation of elastic spin and related intriguing phenomena paves a new way for chiral elasticity, miniature on-chip devices, and spin-sensitive sensors.

Spin angular momentum (SAM) provides fundamental understanding of symmetrical and topological properties of physics [1–3], from quantum to classical aspects [4–6]. It allows people to realize robust one-way edge states propagating with spin-selected direction in what is known as topological insulator [7, 8]. While in classical wave systems, an analogy degree of freedom called pseudo-spin is proposed by carefully designing the meta-structures, such as in electromagnetism [9–14] and acoustics [15–21], so that a pseudo time-reversal symmetry can be realized in the mathematical sense to implement the pseudo-spin-dependent topological phenomena. In particular, in the field of elastic topological metamaterials, the pseudo-spin has been synthesized by joining two degenerate degrees of freedom mathematically, such as using two inter-coupled vibrating oscillators [22], combing symmetric and antisymmetric elastic modes [23, 24], exploiting double degenerated Dirac cones [25, 26], and extracting elastic vortex feature with two valley degrees of freedom [27].

Different from aforementioned pseudo-spin, intrinsic spin of elastic waves has been uncovered by the real physical quantity SAM that corresponds to the rotation of displacement polarization in general solid structures [28]. Moreover, non-reciprocal elastic-magnetic dynamics have been reported in spin-based on-chip magnetic devices and sensors [29, 30], indicating that the elastic spin may even play a significant role in the magnetic dynamics through elastic-magnetic couplings. Yet, so far the direct experimental observation of elastic spin is still absent. Due to the large acoustic impedance, high operation frequency and low vibration amplitude of elastic wave in solid materials, it is inevitably challenging to build an ultra-

sonic chiral source with sufficient radiation power, not even to mention the observation of rotating displacement polarization.

Here, by characterizing the displacement field and SAM on conventional metal plate upon the ultrasonic chiral meta-sources, we report the observation of intrinsic elastic spin and experimental demonstration of its basic properties, including the spin-resolved wave mode and the deterministic spin-momentum locked one-way propagation. The results advance the understanding of elastic spin and broadband spin-dependent properties in general solids, provide people more possibility and flexibility to design the on-chip elastic device [25–27], and pave a way for further revealing new phenomena of chiral elasticity [31–33], spin transfer [34] and conversion in coupled multi-physical systems [29, 30].

Principle of elastic spin and chiral meta-sources. We first focus on chiral Rayleigh wave that exhibits tight spin-momentum locking on the free surface of semi-infinite solid. The displacement vector of surface Rayleigh wave is elliptically polarized, whose SAM density is described by the elastic spin [28], as:

$$\mathbf{S} = \frac{\rho\omega}{2} \text{Im}[\mathbf{u}^* \times \mathbf{u}], \quad (1)$$

where ρ is the density of elastic medium, ω denotes the circular frequency, and $\mathbf{u} = \{u_x, u_y, u_z\}$ is the displacement vector. It should be noted that the elastic SAM describes a local rotating polarization in time domain rather than the vorticity of a displacement field along x or $-x$ in space domain.

As shown in Fig. 1(a), a chiral elastic source whose spin is positive (resp. negative) can only excite the left-going (resp. right-going) wave that has the positive (resp. negative) elastic SAM. This tight coupling between SAM and propagating direction of Rayleigh wave can be understood according to

* These two authors contributed equally to this work.

† Corresponding address: jinfeng.zhao@tongji.edu.cn

‡ Corresponding address: Xonics@tongji.edu.cn

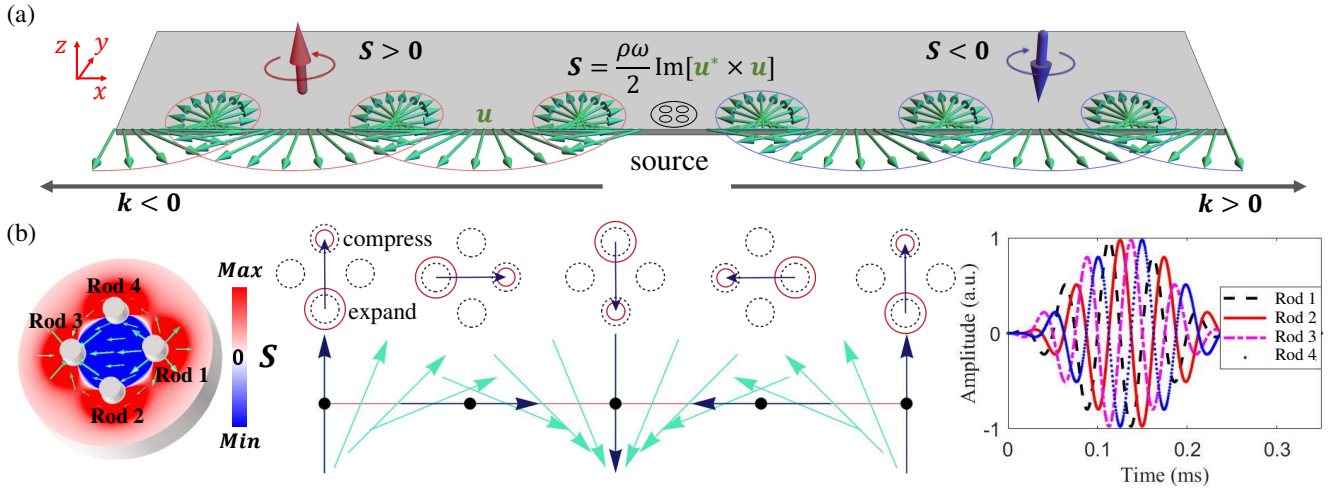


FIG. 1. **Schematic diagram of elastic spin and chiral meta-sources for surface elastic wave.** (a) Illustration of elastic spin of chiral Rayleigh wave. The green vectors show the displacement polarization \mathbf{u} for both the left-going ($\mathbf{k} < 0$) and right-going ($\mathbf{k} > 0$) Rayleigh wave on top of semi-infinite solid. The thick red/blue arrows denote the positive/negative SAM of surface wave, which describes the spiralling of displacement field. (b) Scheme of chiral elastic source with positive spin. The left panel shows the SAM distribution of the synthesized spin-up source with input signals loaded on Rod 1 to 4, respectively. The red/blue color denotes the positive/negative elastic SAM in the outer/inner area. The green arrows denotes the snapshot of displacement vector at a particular moment. The middle panel presents the time evolution (from left to right) of the displacement polarization at the center of the spin-up source. During each period, the displacement vector between four rods rotates one cycle, as shown by the black arrows. The right panel shows the input five-cycled tone burst signals for spin-up source, with an incremental $\pi/2$ -phase delay from Rod 1 to 4.

70 Rayleigh wave equation (see Methods, Eq. 3), i.e. the positive
 71 (resp. negative) \mathcal{S} along z -axis only supports negative (resp.
 72 positive) wave vector \mathbf{k} along x -axis. Consequently, the one-
 73 way Rayleigh wave can be selectively excited by the elastic
 74 sources with chirality.

75 To construct such an effectively chiral elastic source in
 76 solids applicable for broad ultrasonic frequency regime, we
 77 elaborately design an array of sub-wavelength meta-sources
 78 with clockwise or anticlockwise phase shift, as shown in the
 79 left panel of Fig. 1(b), instead of adopting the macroscopic
 80 mechanical stirring in soft matters [32]. The chiral meta
 81 source constitutes four breathing rods labeled with Rod 1 to
 82 Rod 4. The displacement vectors around a single rod all point
 83 to the rod center or all away from the rod center, which allows
 84 the polarization of displacement vector to be always opposite
 85 between the inner and outer area. As such, the sign of SAM is
 86 opposite between the inner and outer area of the chiral meta-
 87 sources. Considering the elastic meta-sources couples with
 88 neighboring field through its outer area, we call the source
 89 whose elastic SAM in outer area is positive as spin-up source
 90 while the negative one as spin-down source. To set rods into
 91 breathing vibration, we symmetrically fix a PZT ring on two
 92 laterals of each rod (Supplementary Fig. S1). To distinguish
 93 the initial wave package from the reflected one, the five-cycled
 94 tone burst pulse signal, as shown in right panel of Fig. 1(b), is
 95 simultaneously imposed on the PZT ring pair from Rod 1 to 4
 96 in order. The input signal phase difference, being $\pi/2$ versus
 97 the central frequency of burst signals, is adjusted between Rod
 98 1 to 4 in the clockwise or anticlockwise way to get spin-down
 99 or spin-up source, respectively.

100

Observation of elastic spin for chiral Rayleigh wave.

101 Fig. 2(a) shows the experimental setup whereby the chiral
 102 elastic meta-sources is implemented around center $(x, y) =$
 103 $(0, 1.2 \text{ cm})$. Fig. 2(b) shows the measured spatiotemporal pat-
 104 tern of u_y (top panel) and the mapped FFT component (bot-
 105 tom panel) at each point around the central frequency 28 kHz.
 106 Obviously, the spin-up source prefers to excite Rayleigh wave
 107 with negative \mathbf{k} , while the spin-down source mainly gener-
 108 ates Rayleigh wave with positive \mathbf{k} . These results are con-
 109 sistent with theory (see Methods), magnifying the tight cou-
 110 pling between the source spin and the propagating direction of
 111 Rayleigh wave, as well as the elastic SAM of Rayleigh wave
 112 itself. Similar results are confirmed in simulation results, as
 113 shown in Supplementary Fig. S2.

114 Quantitatively, the left panel of Fig. 2(c) presents the rec-
 115 tified amplitude of $|u_y|$ of the unidirectional wave upon the
 116 spin-down and spin-up source on free surface ($y = 0$). Un-
 117 ambiguously, the larger $|u_y|$ occurs at $x < 0$ side when using
 118 spin-up source (red) but shifts to $x > 0$ side with spin-down
 119 source (blue). We then tune the central frequency of input
 120 signal, modify the phase difference, and measure the out-of-
 121 plane displacement from $x = -55$ to -25 cm ($u_{y(x<0)}$) and
 122 $x = 25$ to 55 cm ($u_{y(x>0)}$) within a broad ultrasonic fre-
 123 quency range. In Fig. 2(c), right panel shows that the rectifica-
 124 tion ratio of $|u_{y(x<0)}/u_{y(x>0)}|$ (red, spin-up source) and its counter-
 125 part of $|u_{y(x>0)}/u_{y(x<0)}|$ (blue, spin-down source) are always
 126 larger than 1 in the working frequency range.

127 Fig. 2(d) then shows the normalized 2D-FFT component of

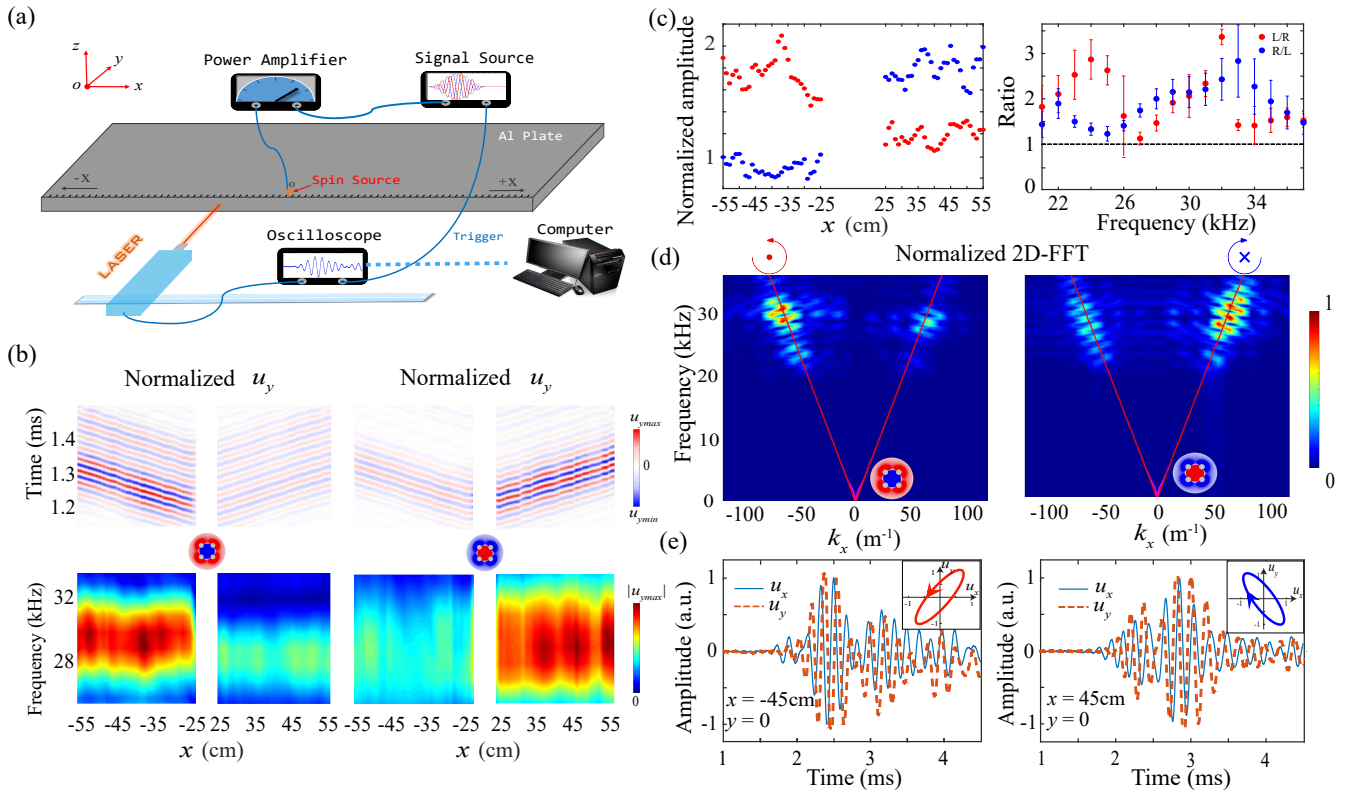


FIG. 2. Experimental observation of elastic spin and chiral selection of Rayleigh mode. (a) Schematic of measurement setup. The plate thickness (along y axis) is effectively infinite, much larger than the skin depth of Rayleigh wave in ultrasonic frequency range 21 ~ 37 kHz. Rayleigh wave is observed by characterizing the out-of-plane displacement u_y on x - z surface. (b) The mapping of normalized u_y measured by laser Doppler vibrometer (see Methods) along the segment ($x = -55 \sim -25$ cm and $x = 25 \sim 55$ cm every 1 cm) in time (top panels) and frequency (bottom panels) domain, and they present the amplitude of Rayleigh wave with negative or positive k_x , respectively. The elastic SAM of excited source is positive (left panels) and negative (right panels), respectively. The rectified amplitude of the $|u_y|$ along x axis at 28 kHz (left panel), which all normalized to the $|u_y|$ recorded at point $x = -55$ cm with spin-down source. The red and blue dots represent results with spin-up and spin-down sources, respectively. The right panel shows the average ratios of measured $|u_y|$ at $x = -55 \sim -25$ cm and $x = 25 \sim 55$ cm, in a broad ultrasonic frequency regime. The red dots are for the $|u_{y(x<0)}/u_{y(x>0)}|$ when using spin-up source while the blue dots stands for $|u_{y(x>0)}/u_{y(x<0)}|$ with the spin-down source. The bars at each frequency are defined as the average ratio plus and/or subtract standard deviation of ratios derived at every group of points. The difference between two rectification ratio profiles comes from the imperfection of chiral sources during the manual installation. (d) Normalized 2D-FFT component of Rayleigh wave with the spin-up (left panel) or spin-down source (right panel) with $f_c = 28$ kHz, correspondingly. The red solid line is the theoretical dispersion for Rayleigh wave branch on semi-infinite aluminum solid. The red and blue circular arrows show the spin direction of the left- and right-going waves. (e) The time evolution of u_x (blue solid line) and u_y (red dash line) measured at $x = -45$ cm (left panel) and $x = 45$ cm (right panel) when using spin-up or spin-down source, respectively, normalized to the maximum amplitude of themselves. By extracting FFT components, i.e. amplitude and phase information, from displacement signals $u_x(t)$ and $u_y(t)$ at particular frequency, the elastic SAM is obtained in experiment. The insets show the anti-clockwise (left panel) and clockwise (right panel) rotation of displacement polarization $\mathbf{u} = (u_x, u_y)$.

132 measured u_y with input signal frequency centered at 28 kHz,
 133 which are well matched to theoretical Rayleigh wave branch
 134 (red solid line). The left (resp. right) panel is obtained when
 135 excited with spin-up (resp. down) source and presents higher
 136 energy density on the left (resp. right) branch, respectively.
 137 Similar phenomena are observed when input signals are tuned
 138 in the broad frequency range 21 ~ 37 kHz. It is worth em-
 139 phasizing that here not only the source chirality but also the
 140 SAM of the chiral wave itself is tightly locked to the wave
 141 propagation direction.

142 We further measure the SAM of chiral Rayleigh wave to
 143 confirm the spin-momentum locking. To this end, we perfo-

144 rate small V-shape grooves in the surface of plate to obtain
 145 the out-of-plane displacement u_y and the in-plane displace-
 146 ment u_x (Supplementary Fig. S1 (c) for details). Fig. 2(e)
 147 shows the measured temporal profiles of normalized u_x and
 148 u_y at position $x = -45$ cm (left panel, spin-up source) or $x =$
 149 45 cm (right panel, spin-down source). Clearly, the phase of
 150 u_x (blue solid line) at $x = -45$ cm is earlier than the one of u_y
 151 (red dash line). The inset shows the anticlockwise rotation of
 152 displacement polarization \mathbf{u} which corresponds to a positive
 153 \mathcal{S} . The situation is reversed with spin-down source excita-
 154 tion, where the phase of u_x at $x = 45$ cm is later than that of
 155 u_y while the rotation direction of polarization \mathbf{u} is clockwise,

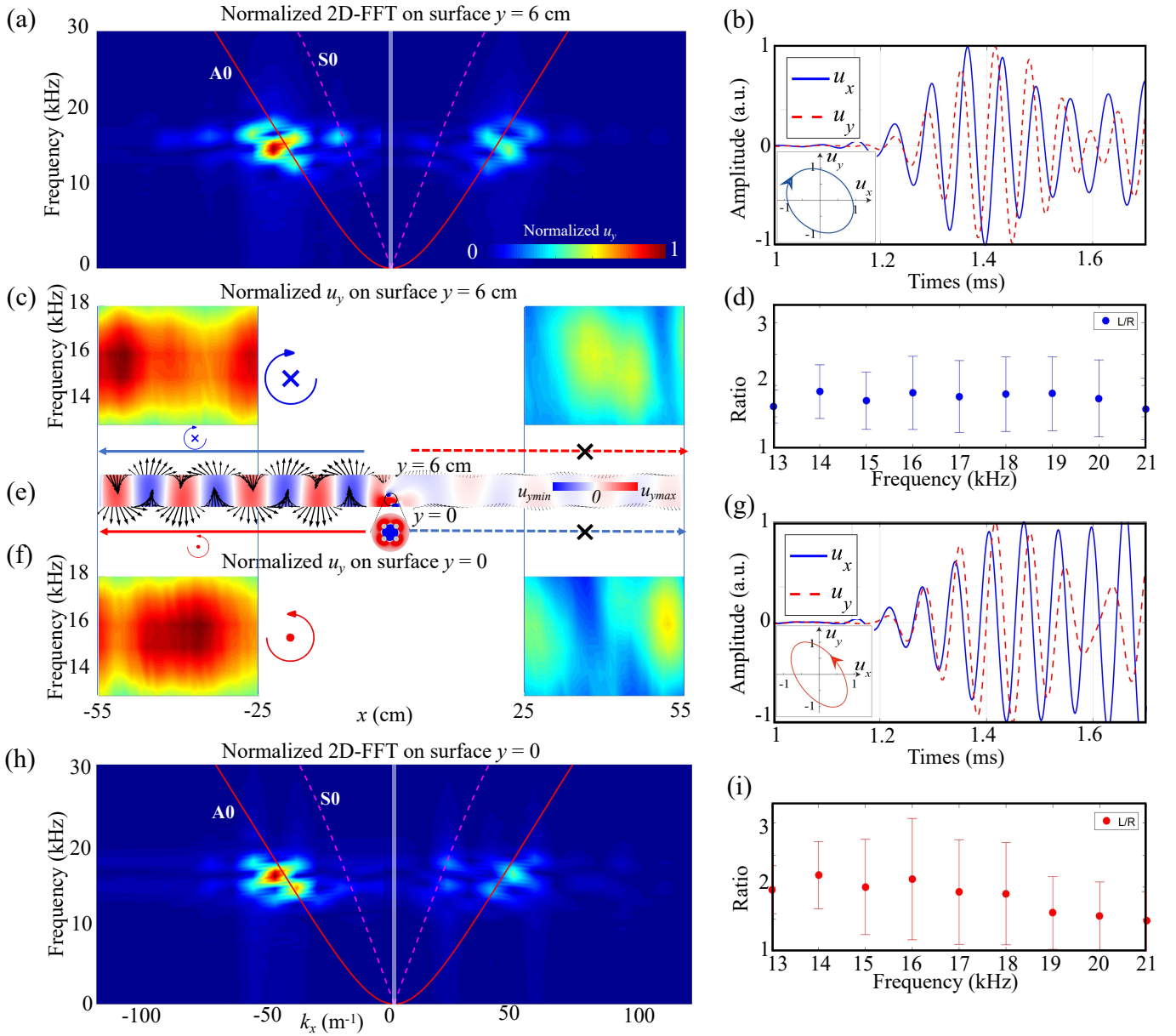


FIG. 3. Experimental observation of elastic spin and chiral selection of antisymmetric Lamb wave. (a, h) 2D-FFT components of measured amplitudes for the chiral Lamb waves on back surface $y = 6$ cm and front surface $y = 0$, respectively, upon the spin-up source. Here a 6 cm thick aluminum plate that occupies $y = 0 \sim 6$ cm along y axis (depth direction) is chosen as the experimental sample, as shown in Supplementary Fig. S1 (a). And the chiral source is implemented at $(x, y) = (0, 1.2)$ cm, near the front surface $y = 0$. Red solid and magenta dash lines stand for the theoretical dispersion of A_0 and S_0 wave branches in a 6 cm thick aluminum plate, respectively. Both densities of state significantly locate on the left A_0 wave branch, indicating the chiral selective excitation of one-way A_0 mode. (b, g) The time evolution of u_x (blue solid line) and u_y (red dash line) measured at $x = -45$ cm on surfaces $y = 6$ cm and $y = 0$, respectively, when using spin-up source. The insets show their corresponding clockwise and anti-clockwise rotation of displacement polarization \mathbf{u} at frequency 14 kHz, for left-going wave. As such, the positive SAM of chiral source couples with the positive elastic SAM at front surface, which leads to the left-going A_0 wave. (c, f) Normalized FFT of u_y measured along $x = -55 \sim -25$ cm and $x = 25 \sim 55$ cm every 1 cm on back surface $y = 6$ cm and front surface $y = 0$, respectively. Leftward unidirectional propagation is clearly observed in a broad frequency range, but with the opposite rotating polarizations of \mathbf{u} and opposite elastic SAM at two surfaces for the left-going A_0 wave (clockwise and negative \mathcal{S} at the back, while anti-clockwise and positive \mathcal{S} at the front). (d, i) The average ratios of measured $|u_y|$ at $x = -55 \sim -25$ cm and $x = 25 \sim 55$ cm, in a broad ultrasonic frequency regime. The dots are for the $|u_{y(x<0)}|/|u_{y(x>0)}|$ with spin-up source on surface $y = 6$ cm (d) and $y = 0$ (i). (e) Simulated unidirectional A_0 wave upon the chiral source excitation propagates mainly towards left side with opposite elastic SAM on two parallel surfaces at $y = 0$ and $y = 6$ cm, which confirms the experimental observations.

tion at $x = \pm 45$ cm is recorded by alternatively using two spin sources for the convenience of illustration. Considering the measured unidirectional wave propagation and the obtained signs of \mathbf{S} at both $x < 0$ and $x > 0$ sides, we find that the opposite unidirectional wave carries opposite elastic spin and the dispersion of Rayleigh wave in Fig. 2(d) is spin-resolved in the broad frequency regime. The chiral selection of one-way propagation relies on the angular momentum matching between the source spin and the elastic spin of wave itself on particular direction, which clearly demonstrates the spin-momentum locking effect (see Methods).

Observation of elastic spin for chiral Lamb wave. We next turn to investigate the elastic spin and spin-momentum locking for the lowest-order antisymmetric Lamb (A_0) wave. Different from Rayleigh wave, A_0 wave contains a couple of opposite SAM on surfaces $y = 0$ and $y = 6$ cm (see Methods, Eqs. 4 and 5), e.g. the left-going wave possess negative SAM at the back surface $y = 6$ cm due to the antisymmetric nature of A_0 wave, as shown in Fig. 3(e). To demonstrate this point, we carried out measurement on both surfaces where u_y is recorded for both the left ($x = -55 \sim -25$ cm) and right ($x = 25 \sim 55$ cm) sides every 1 cm. When using the spin-up source with central excitation frequency 14 kHz, Figs. 3(a) and (h) illustrate the normalized 2D-FFT components of $|u_y|$ on the back and front surfaces, respectively. Evidently, the components are very large for A_0 wave but very minor for the lowest-order symmetric Lamb (S_0) wave, which confirms the efficient generation of A_0 wave. The primary density-of-state spot overlaps on the left A_0 branch over its right counterpart, showing the SAM-dependent coupling between the spin-up source and A_0 wave with negative \mathbf{k} on surface $y = 0$. The FFT component of $|u_y|$ on surfaces $y = 0$ and $y = 6$ cm in space domain are shown in Figs. 3(f) and (e), respectively, magnifying also the tight spin-momentum locking effect. These are well consistent with the numerical results in Fig. 3(e) and theoretical results derived from A_0 wave equation (see Methods, Eqs. 4 and 5).

To observe the elastic spin in chiral A_0 wave, small V-shape grooves are also truncated on the x - z surfaces at $y = 0$ and $y = 6$ cm. As such, we can measure the SAM profiles from the temporal signals of displacements u_x and u_y , shown in Figs. 3(b) and (g). The displacement polarizations at $x = -45$ cm on the back and front surfaces are shown by insets of Figs. 3(b) and (g), respectively. The rotations of displacement polarization are the same in the excited wave on $y = 0$ and in the outer area of chiral source, being akin to the SAM matching between chiral source and Rayleigh wave mode. Furthermore, the measurement demonstrates the positive \mathbf{S} at front surface $y = 0$ and negative \mathbf{S} at back surface $y = 6$ cm, which confirms the opposite SAM between two surfaces indicated by Eqs. 4 and 5. This phenomenon is absent in Rayleigh wave but unique for Lamb wave system.

Relevant results of chiral selective generation of right-going A_0 wave, by using the spin-down source, is demonstrated in Supplementary Fig. S3. Lastly but importantly, the chiral selective routing of A_0 wave is dependent on the elastic spin of wave itself, and occurs in a broad frequency range whenever using the spin-up or spin-down source, as shown in

Figs. 3(d) and (i) and Supplementary Fig. S4.

Discussion

In conventional solid structures, we have experimentally demonstrated the intrinsic spin in elastic waves, by measuring the SAM according to the rotating displacement polarization in Eq. 1. The chiral selective excitation of unidirectional wave propagation has been observed in experiments for both Rayleigh and Lamb wave systems without the help of any meta-structure, but by using the elaborately designed elastic chiral meta-sources. In particular, the tight spin-momentum locking is confirmed by the fact that the locally rotating displacement polarizations of the surface wave field itself determines the propagating direction. Moreover, we have observed the opposite elastic spin carried by the one-way Lamb wave on two-side surfaces in addition to the source chirality. These results agree well with the theoretical predictions and numerical simulations, in broad ultrasonic frequency ranges. The experimental observation of elastic spin demonstrates the validity and feasibility of intrinsic spin angular momentum in elasticity, which offers a promising platform for future investigation on integrative spin physics among electron [35], phonon [36], photon [4], and magnon [29, 30, 34], and provides new perspectives and means to the integrative on-chip surface-acoustic-wave devices that have shown the great potential in quantum acoustics [37, 38].

Methods

The displacement field of Rayleigh wave in x - y plane can be expressed as:

$$\begin{aligned} u_x &= iAk_R \left(e^{-\kappa_l y} - \frac{2\kappa_l \kappa_t}{k_t^2} e^{-\kappa_t y} \right) e^{i(k_R x - \omega t)}, \\ u_y &= -Ak_l \left(e^{-\kappa_l y} - \frac{2\kappa_R^2}{k_t^2} e^{-\kappa_t y} \right) e^{i(k_R x - \omega t)}, \end{aligned} \quad (2)$$

where ρ is mass density, ω is circular frequency, A is wave amplitude, and k_R is the x -component of Rayleigh wave vector. k_l and k_t are the wave numbers of longitudinal and transverse waves in bulk solid, respectively, whereas the $\kappa_l = \sqrt{k_l^2 - k_R^2}$ and $\kappa_t = \sqrt{k_t^2 - k_R^2}$. By combining $\mathbf{S} = \frac{\rho\omega}{2} \text{Im}[\mathbf{u}^* \times \mathbf{u}]$ with Eq. 3, one can obtain the SAM of Rayleigh wave at $y = 0$:

$$\mathbf{S}_R = -k_R \kappa_l \rho \omega A^2 \frac{(k_R^2 - \kappa_t^2)(k_R^2 + \kappa_t^2 - 2\kappa_l \kappa_t)}{(k_R^2 + \kappa_t^2)^2}. \quad (3)$$

Obviously, the sign of \mathbf{S}_R is tightly correlated with the sign of k_R when $y = 0$, which shows the spin-momentum locking of Rayleigh wave.

For a plate that traverses from $y = 0$ to $y = d$, the SAM of A_0 wave propagating in this plate is:

$$\begin{aligned} \mathbf{S}_{A_0} &= -k_{A_0} \kappa_l \rho \omega A^2 \frac{k_{A_0}^2 - \kappa_t^2}{k_t^4} \cosh\left(\frac{\kappa_l d}{2}\right) \left[k_t^2 \sinh\left(\frac{\kappa_l d}{2}\right) \right. \\ &\quad \left. - 2\kappa_l \kappa_t \cosh\left(\frac{\kappa_l d}{2}\right) \tanh\left(\frac{\kappa_t d}{2}\right) \right] \end{aligned} \quad (4)$$

at $y = 0$, but becomes:

$$\begin{aligned} \mathcal{S}_{A_0} = & k_{A_0} \kappa_l \rho \omega A^2 \frac{k_{A_0}^2 - \kappa_t^2}{k_t^4} \cosh\left(\frac{\kappa_l d}{2}\right) \left[k_t^2 \sinh\left(\frac{\kappa_l d}{2}\right) \right. \\ & \left. - 2\kappa_l \kappa_t \cosh\left(\frac{\kappa_l d}{2}\right) \tanh\left(\frac{\kappa_t d}{2}\right) \right] \end{aligned} \quad (5)$$

at $y = d$. A is wave amplitude, k_{A_0} is the x -component of wave vector of A_0 mode. k_l and k_t are the wave numbers of longitudinal and transverse waves in bulk medium, whereas the $\kappa_l = \sqrt{k_l^2 - k_{A_0}^2}$ and $\kappa_t = \sqrt{k_t^2 - k_{A_0}^2}$. The plate thickness is d . Clearly, $\mathcal{S}_{A_0}(y = 0) = -\mathcal{S}_{A_0}(y = d)$. The sign

of \mathcal{S}_{A_0} is tightly correlated with the sign of k_{A_0} , which shows the spin-momentum locking of A_0 wave.

Data availability

The data that support the findings of this study are available from the corresponding author upon reasonable request.

Acknowledgments

This work is supported by the National Natural Science Foundation of China (Nos. 11935010 and 11775159), the Shanghai Science and Technology Committee (Nos. 18JC1410900 and 20ZR1462700), and the Opening Project of Shanghai Key Laboratory of Special Artificial Microstructure Materials and Technology.

-
- [1] K. Y. Bliokh, D. Smirnova, and F. Nori, *Science* **348**, 1448 (2015).
- [2] K. Y. Bliokh, F. J. Rodríguez-Fortuño, F. Nori, and A. V. Zayats, *Nat. Photonics* **9**, 796 (2015).
- [3] A. Aiello, P. Banzer, M. Neugebauer, and G. Leuchs, *Nat. Photonics* **9**, 789 (2015).
- [4] P. Lodahl, S. Mahmoodian, S. Stobbe, A. Rauschenbeutel, P. Schneeweiss, J. Volz, H. Pichler, and P. Zoller, *Nature* **541**, 473 (2017).
- [5] K. Y. Bliokh and F. Nori, *Phys. Rep.* **592**, 1 (2015).
- [6] K. Y. Bliokh, A. Y. Bekshaev, and F. Nori, *Nat. Commun.* **5**, 3300 (2014).
- [7] M. Z. Hasan and C. L. Kane, *Rev. Mod. Phys.* **82**, 3045 (2010).
- [8] X.-L. Qi and S.-C. Zhang, *Rev. Mod. Phys.* **83**, 1057 (2011).
- [9] L. Lu, J. D. Joannopoulos, and M. Soljačić, *Nat. Photonics* **8**, 821 (2014).
- [10] W.-J. Chen, Z.-Q. Zhang, J.-W. Dong, and C. T. Chan, *Nat. Commun.* **6**, 8183 (2015).
- [11] C. He, X.-C. Sun, X.-P. Liu, M.-H. Lu, Y. Chen, L. Feng, and Y.-F. Chen, *PNAS* **113**, 4924 (2016).
- [12] Y. Yang, Y. F. Xu, T. Xu, H.-X. Wang, J.-H. Jiang, X. Hu, and Z. H. Hang, *Phys. Rev. Lett.* **120**, 217401 (2018).
- [13] Y. Li, Y. Sun, W. Zhu, Z. Guo, J. Jiang, T. Kariyado, H. Chen, and X. Hu, *Nat. Commun.* **9**, 4598 (2018).
- [14] Y. Yang, Z. Gao, H. Xue, L. Zhang, M. He, Z. Yang, R. Singh, Y. Chong, B. Zhang, and H. Chen, *Nature* **565**, 622 (2019).
- [15] G. Ma, M. Xiao, and C. T. Chan, *Nat. Rev. Phys.* **1**, 281 (2019).
- [16] Z. Yang, F. Gao, X. Shi, X. Lin, Z. Gao, Y. Chong, and B. Zhang, *Phys. Rev. Lett.* **114**, 114301 (2015).
- [17] J. Lu, C. Qiu, M. Ke, and Z. Liu, *Phys. Rev. Lett.* **116**, 093901 (2016).
- [18] Z. Zhang, Q. Wei, Y. Cheng, T. Zhang, D. Wu, and X. Liu, *Phys. Rev. Lett.* **118**, 084303 (2017).
- [19] C. He, S.-Y. Yu, H. Wang, H. Ge, J. Ruan, H. Zhang, M.-H. Lu, and Y.-F. Chen, *Phys. Rev. Lett.* **123**, 195503 (2019).
- [20] C. He, H.-S. Lai, B. He, S.-Y. Yu, X. Xu, M.-H. Lu, and Y.-F. Chen, *Nat. Commun.* **11**, 2318 (2020).
- [21] Z. Tian, C. Shen, J. Li, E. Reit, H. Bachman, J. E. S. Socolar, S. A. Cummer, and T. Jun Huang, *Nat. Commun.* **11**, 762 (2020).
- [22] R. Süssstrunk and S. D. Huber, *Science* **349**, 47 (2015).
- [23] S. H. Mousavi, A. B. Khanikaev, and Z. Wang, *Nat. Commun.* **6**, 8682 (2015).
- [24] M. Miniaci, R. K. Pal, B. Morvan, and M. Ruzzene, *Phys. Rev. X* **8**, 031074 (2018).
- [25] J. Cha, K. W. Kim, and C. Daraio, *Nature* **564**, 229 (2018).
- [26] S.-Y. Yu, C. He, Z. Wang, F.-K. Liu, X.-C. Sun, Z. Li, H.-Z. Lu, M.-H. Lu, X.-P. Liu, and Y.-F. Chen, *Nat. Commun.* **9**, 3072 (2018).
- [27] M. Yan, J. Lu, F. Li, W. Deng, X. Huang, J. Ma, and Z. Liu, *Nat. Mater.* **17**, 993 (2018).
- [28] Y. Long, J. Ren, and H. Chen, *PNAS* **115**, 9951 (2018).
- [29] J. Holanda, D. S. Maior, A. Azevedo, and S. M. Rezende, *Nat. Phys.* **14**, 500 (2018).
- [30] M. Xu, K. Yamamoto, J. Puebla, K. Baumgaertl, B. Rana, K. Miura, H. Takahashi, D. Grundler, S. Maekawa, and Y. Otani, *Sci. Adv.* **6**, eabb1724 (2020).
- [31] T. Frenzel, M. Kadic, and M. Wegener, *Science* **358**, 1072 (2017).
- [32] M. Lanoy, F. Lemoult, A. Eddi, and C. Prada, *PNAS* **117**, 30186 (2020).
- [33] H. Nassar, Y. Y. Chen, and G. L. Huang, *Phys. Rev. Lett.* **124**, 084301 (2020).
- [34] T. Kawada, M. Kawaguchi, T. Funato, H. Kohno, and M. Hayashi, *Sci. Adv.* **7**, eabd9697 (2021).
- [35] I. Žutić, J. Fabian, and S. Das Sarma, *Rev. Mod. Phys.* **76**, 323 (2004).
- [36] N. Li, J. Ren, L. Wang, G. Zhang, P. Hänggi, and B. Li, *Rev. Mod. Phys.* **84**, 1045 (2012).
- [37] K. J. Satzinger, Y. P. Zhong, H. S. Chang, G. A. Peairs, A. Bienenfait, M.-H. Chou, A. Y. Cleland, C. R. Conner, E. Dumur, J. Grebel, I. Gutierrez, B. H. November, R. G. Povey, S. J. Whiteley, D. D. Awschalom, D. I. Schuster, and A. N. Cleland, *Nature* **563**, 661 (2018).
- [38] R. Manenti, A. F. Kockum, A. Patterson, T. Behrle, J. Rahamim, G. Tancredi, F. Nori, and P. J. Leek, *Nat. Commun.* **8**, 975 (2017).

Supplementary Files

This is a list of supplementary files associated with this preprint. Click to download.

- [Supp.pdf](#)